2 (2026) 100042

Contents lists available at ScienceDirect

Biomass Futures

journal homepage: www.sciencedirect.com/journal/biomass-futures

Lead ion removal from aqueous solutions using biochar materials from different wood species

Ruiqi Li [a], Tara Keyser [b], Thomas Elder [a], Qiangu Yan [c], Zhiyong Cai [c], Yucheng Peng [a,*]

[a] College of Forestry, Wildlife, and Environment, Auburn University, Auburn, AL, USA
[b] USDA-Forest Service, Southern Research Station, Asheville, NC, USA
[c] USDA-Forest Service, Forest Products Laboratory, Madison, WI, USA

ARTICLE INFO

Keywords:
Wood
Biochar
Lead ion
Pyrolysis

ABSTRACT

Heavy metal contamination in water systems driven by industrialization and urbanization is a primary concern for society. The development of efficient remediation methods to reduce heavy metal contamination in water is necessary. Biochar has emerged as a promising adsorbent for heavy metals due to its unique physicochemical properties. This study investigated the effect of biochars manufactured from 12 different wood species on lead ion (Pb(II)) removal capacity in aqueous solutions. The 12 different wood species include two softwoods and 10 hardwoods. The physicochemical properties and the lead ion adsorption capacity of biochars were characterized. The Pb(II) removal capacity of biochars derived from hardwoods was significantly higher than that of softwood-derived biochars. Among the hardwoods, aspen biochar exhibited the highest removal capacity (42.7 mg g^{-1}), which can be attributed to its higher $CaCO_3$ content compared to softwood feedstocks. These results indicate that feedstock type plays a critical role in determining the physicochemical properties of biochar and its performance in Pb(II) removal. Overall, hardwoods are more suitable feedstocks for producing biochars intended for lead-contaminated water treatment.

1. Introduction

Rapid urbanization and industrialization have raised substantial environmental concerns, particularly about water quality [1,2]. With the acceleration of population growth, the expansion of industrial activities and urban development has become a primary factor in water pollution [3]. Water pollution is especially exacerbated by elevated concentrations of heavy metals in lakes, rivers, groundwater, and other water sources [4]. This contamination results from various anthropogenic activities, including the release of mine tailings, disposal of metal-laden wastes, expansion of industrial areas, and the use of lead paints, especially in developing countries [3,5]. Zhou et al. [5] analyzed global heavy metal contamination across 168 rivers and 71 lakes between 1972 and 2017, revealing significant spatiotemporal patterns. Specifically, heavy metal concentrations and the frequency of levels exceeding the safety thresholds set by the World Health Organization (WHO) and the United States Environmental Protection Agency (EPA) increased markedly over time. Mean concentration levels and the number of metals exceeding safety limits, such as lead (Pb), cadmium (Cd), and chromium (Cr), rose sharply from the 1990s onward. During the 1990-2010s, eight to ten metals exceeded thresholds, compared to two to four metals in the 1970s and 1980s. Notably, Pb concentrations rose from 9.38 ± 4.60 μg L^{-1} in the 1970s to 116.13 ± 25.84 μg L^{-1} in the 2010s, exceeding the WHO guideline limit of 10 μg L^{-1} by more than 11-fold. Spatially, developing regions including Africa, Asia, and South America showed elevated contamination. For example, Pb concentrations reached 332.93 μg L^{-1} in South America compared to 14.31 μg L^{-1} in European waters. Pollution sources shifted from mining and manufacturing (accounting for 66.0% of total contribution in the 1970s) to waste discharge and rock weathering (accounting for 97.4% in the 2000s). Regional drivers varied considerably, with agricultural inputs representing the largest source in Africa at 56.7%, whereas industrial activities dominated in Asia at 97.1% [5]. These findings highlight the urgent need for effective heavy metal pollution mitigation strategies.

Heavy metals are naturally occurring elements characterized by a density greater than 5 g cm^{-3}, an atomic number greater than 20, and high toxicity [6]. In humans, exposure to heavy metals can cause liver and kidney damage, neurological and cardiovascular disorders, carcinogenicity, and disruption of endocrine and immune functions [7,8]. In ecosystems, they impair plant growth, reduce microbial diversity, and

* Corresponding author.
E-mail address: yzp0027@auburn.edu (Y. Peng).

https://doi.org/10.1016/j.bmf.2026.100042
Received 21 February 2026; Received in revised form 2 April 2026; Accepted 7 April 2026
Available online 8 April 2026

disrupt the behavioral, biochemical, and reproductive functions of aquatic organisms [7]. In aquatic systems, metallic contaminants predominantly exist as inorganic ions (e.g., Zn (II), Cd (II), Pb(II), CrO_4(-II), Fe (II)/Fe (III)), with their chemical forms governed by pH, redox potential, and ligand interactions with hydroxides, carbonates, or sulfates [9]. Environmental dynamics drive metal-specific transformations: zinc persists as Zn (II) in acidic waters [10], lead transitions between Pb(II) cations and hydroxyl complexes (e.g., $Pb(OH)^+$) under alkaline conditions [11], while chromium shifts from Cr (III) in reducing zones to Cr (VI) as chromate in oxidizing regimes [12]. These metals exhibit three forms governing ecotoxicity: (1) free hydrated ions, (2) ligand-stabilized complexes, and (3) colloidal precipitates or adsorbed phases [9]. The ecotoxicity of these forms depends primarily on their bioavailability. Among them, free hydrated ions, which represent the first form, are the most bioavailable and toxic. Ligand-stabilized complexes, the second form, show intermediate bioavailability and toxicity. The least toxic are colloidal precipitates or adsorbed phases (form 3), as their large size and solid-state nature limit biological uptake [9]. In addition, heavy metals are non-biodegradable and persist indefinitely in the environment, contaminating air, water, and soil. Given their long-term persistence and toxicity, effective pollution control strategies are needed to reduce their bioavailability, mobility, and overall toxicity through adsorption, complexation, or precipitation [13].

To mitigate heavy metal contamination in water, various treatment technologies have been developed, broadly categorized into physicochemical (e.g., adsorption, ion exchange, membrane filtration, and flotation), chemical (e.g., precipitation, redox, and electrochemistry), and biological (e.g., phytoremediation, microbial remediation, and biotechnology) methods [14]. Conventional methods such as chemical precipitation, ion exchange, and membrane filtration, though effective under certain conditions, are often limited by high operational costs, risks of secondary pollution, and poor adaptability to low-concentration contaminants [15,16]. For instance, chemical precipitation often relies on adding alkalis (e.g., $Ca(OH)_2$, NaOH) or sulfides agents and generates hazardous sludge containing metal hydroxides or sulfides that require complex disposal [14,17]. Membrane filtration also suffers from high costs and membrane fouling [18]. Although widely used, adsorbents such as the activated carbon produced from coal are high-cost and non-renewable [19]. Therefore, developing efficient, eco-friendly, cost-effective, and sustainable technologies is advantageous.

In this context, biochar has emerged as a promising alternative material for heavy metal removal [20]. Biochar is a carbon-rich material produced by the thermochemical conversion of biomass, derived from abundant and often underutilized feedstocks such as forest residues, agricultural wastes, sewage sludge, or animal manure, which aligns with sustainable economy principles by transforming waste into a functional material [21]. Unlike conventional adsorbents that rely primarily on surface binding, biochar serves as a multifunctional material that facilitates heavy metal immobilization predominantly through chemical precipitation, forming stable insoluble compounds such as $PbCO_3$, complemented by its adsorption capacity [22]. This mechanism differs notably from traditional chemical precipitation, which often relies on adding external reagents and generates hazardous sludge requiring complex disposal. In contrast, precipitates trapped within the porous structure of biochar exhibit greater stability, effectively reducing sludge toxicity and minimizing its volume. The heavy metal removal capacity of biochar results from its physicochemical properties, including high surface area, porous structure, rich surface functional groups, and mineral content, which depend on the raw materials used and how they are processed. Different biomass feedstocks and preparation processes can have a significant impact on these physicochemical properties of biochar, thus affecting its applications in removing heavy metals from aqueous solutions [23–25]. Therefore, the selection of appropriate raw materials and preparation conditions is essential to ensure that biochar serves as an efficient, sustainable, and economically viable strategy for mitigating heavy metal contamination in water.

Woody biomass, composed of lignin, cellulose, and hemicellulose [26,27], offers environmental and economic benefits as a biochar feedstock. Unlike heavy metal-containing wastewater sludge, woody waste minimizes secondary pollution risks due to its simpler chemical composition [28,29]. With the same manufacturing process, woody biochar exhibits higher lignin-derived carbon content, greater specific surface area, and lower ash content compared to herbaceous or crop biochar [30–32]. The global annual production of 4.6 billion tons of wood includes around 920 million tons of underutilized logging residues [33], offering raw material supply for further upgrading to valuable products. In addition, the supply of biomass can be even higher with the occurrence of natural disasters. For example, in 2005, Hurricane Katrina left 619 million ft^3 of softwood debris and 426 million ft^3 of hardwood debris in Mississippi; 287 million ft^3 of softwood and 193 million ft^3 of hardwood in Louisiana; and 126 million ft^3 of softwood and 91 million ft^3 of hardwood in Alabama [34]. Converting such storm-damaged timber and other forest residues into biochar can address three critical issues: (1) carbon sequestration prevents 85 % of the carbon in wood from being broken down and released into the atmosphere [35], (2) wildfire mitigation through flammable debris removal, and (3) economic recovery by value-added biochar production.

In this study, forest feedstocks were utilized for biochar production to investigate the levels of and mechanisms of Pb(II) removal from aqueous solutions. It has been reported in the literature that woody biochar is effective in the removal of Pb(II) [23,36]. Biochar produced from cherry at 600 °C exhibited a Pb(II) removal capacity of 38.8 mg g^{-1} [23], and broadleaf wood biochar prepared at 600 °C also achieved a removal level of 47.61 mg g^{-1} [36]. In contrast, softwood biochar generated at 550 °C showed a much lower Pb(II) removal capacity of 8.07 mg g^{-1} [36]. It is difficult to compare systematically these adsorption capacity data for these biochar samples due to the varying biochar feedstocks and preparation processes used in different studies, preventing a clear understanding of the mechanisms of, and the physical/chemical characteristics of biochar that influence heavy metal removal from solutions. As such, the current study examined biochar produced from 12 native US tree species, determining their physicochemical properties and ability to remove Pb(II) from aqueous solutions. By correlating Pb(II) removal capacities with biochar material property variations, we explored the reaction mechanisms governing Pb(II) removal by woody biochar. These findings provide a scientific basis for selecting appropriate biomass feedstocks to produce biochar as an adsorbent for applications in environmental remediation.

2. Materials and methods

2.1. Reagents

Lead (II) chloride ($PbCl_2$) at a purity of 99% (CAS: 7758-95-4) was purchased from VWR International (Radnor, PA, USA). The solid $PbCl_2$ was dissolved in deionized (DI) water to prepare the $PbCl_2$ solutions with a Pb(II) concentration of 200 mg L^{-1} for biochar adsorption studies. The pH of this solution was approximately 5.0. An identical preparation procedure was used for all solutions to ensure consistent initial concentrations and a uniform pH value. This protocol effectively eliminated variations in the initial solution pH as a potential confounding factor when evaluating the adsorption capacity of the biochar materials.

2.2. Biochar preparation

In this study, 12 wood species were selected as feedstocks for biochar production, comprising 10 hardwoods and two softwoods. The hardwood group encompasses the three major vessel porous patterns: ring-porous species including white oak (*Quercus alba* L.), white ash (*Fraxinus americana* L.), American chestnut (*Castanea dentata* (Marshall) Borkh.), and red oak (*Quercus coccinea* Münchh.); semi-ring-porous represented by pignut hickory (*Carya glabra* (Mill.)); and diffuse-

porous species including red maple (*Acer rubrum* L.), yellow poplar (*Liriodendron tulipifera* L.), black cherry (*Prunus serotina* Ehrh.), birch (*Betula lenta* L.), and quaking aspen (*Populus tremuloides* Michx.). The two softwoods, white pine (*Pinus strobus* L.) and loblolly pine (*Pinus taeda* L.). Wood logs from pignut hickory, red maple, white oak, white ash, yellow poplar, black cherry, American chestnut, red oak, sweet birch, and eastern white pine were collected in disks from the Bent Creek Experimental Forest in the U.S. Forest Service Southern Research Station. The logs were debarked first using a band saw, followed by size reduction into chips. Wood flake samples of quaking aspen were received from USDA-Forest Products Laboratory and loblolly pine was sampled from the Solon Dixon Forestry Education Center, Andalusia, AL. All wood samples were debarked, pre-dried and ground using a blender (7010HS, Waring Products, Torrington, CT, USA). The ground wood particles were sieved through 10-mesh (2 mm) and 40-mesh (0.425 mm) screens to obtain uniformly sized particles that passed through 10-mesh and were retained on top of 40-mesh. The wood particles were stored at room temperature (22 ± 3 °C) in Ziploc bags prior to biochar manufacturing.

Biochar samples from these twelve wood species were prepared using a quartz tube furnace (MTI Corporation GSL-1100X-S, Richmond, CA, USA) under a nitrogen flow rate of 200 $cm^3\ min^{-1}$. The temperature profile used to prepare all the biochar samples in the tube furnace consisted of four sequential steps: (1) a ramp phase from room temperature to 650 °C at 10 °C·min^{-1}, (2) an isothermal retention stage at 650 °C for 60 min, (3) a cooling phase to lower the tube furnace temperature to 200 °C at 5 °C·min^{-1}, and (4) a final cooling stage to reach room temperature. All the operations in the tube furnace were under positive N_2 flow conditions. The biochar samples were weighed and stored in Ziploc bags for the next step of operation.

2.3. Biochar characterization

Biochar characterization was performed using two sample forms: the prepared biochar particles directly after pyrolysis and finely ground biochar powder. Specific surface area, morphology and elemental proportions, pH, and electrical conductivity (EC) were measured using the biochar particles. For elemental composition, ash content, surface functional groups, and crystallinity, the biochar was manually ground using a mortar and pestle and sieved to obtain a fine powder with particle sizes smaller than 106 μm (140 mesh).

The surface morphology and elemental composition of the biochar samples were determined using the ZEISS EVO 10 scanning electron microscopy (SEM, Carl Zeiss AG, Germany) equipped with an energy-dispersive X-ray spectrometer (EDX, EDAX TEAM Element EDS system, USA). The accelerating voltage was set at 20 kV. Three to five particles from each biochar sample were placed on a double-faced adhesive carbon tape to facilitate electron conduction. EDX spectra were collected to identify the elemental distribution on the biochar surface before and after lead ion adsorption.

The specific surface area (SSA) of all the biochar samples was characterized by measuring the CO_2 adsorption isotherm at 0 °C using a Micromeritics TriStar II Plus instrument (Norcross, GA, USA). The biochar samples were degassed first under a vacuum at 200 °C for 24 h using a VacPrep 061 instrument (Micromeritics, Norcross, GA, USA) before the gas adsorption measurement. The CO_2 adsorption isotherms were then fitted with the Dubinin-Astakhov equation [37] to calculate the micropore specific surface area and micropore volume using the software TriStar II Plus 3030 (Norcross, GA, USA). CO_2 adsorption isotherms are better suited than N_2 adsorption for characterizing micropores (<2 nm) in highly disordered biochar materials [38]. This is because N_2 adsorption isotherms (at 77.3 K) primarily characterize meso-/macropores (>2 nm) but are less effective in filling micropores at low temperatures. In contrast, CO_2 adsorption isotherms (at 273 K) utilize the smaller molecular size of CO_2 and higher operational temperature to enhance diffusion kinetics for accurate micropore analysis [37–39]. Measurements of the specific surface area and pore volume for each biochar were performed in triplicate, and their mean values and standard deviations (SD) are reported.

The pH and EC of the biochar samples were determined in a biochar suspension with a biochar to DI water weight ratio of 1:10 [40]. The suspension was prepared by adding 1 g of biochar particles after pyrolysis into 10 mL of DI water in a 50 mL centrifuge tube. The suspension was shaken with a Scilogex Sci-RL-E tube rotator (Rocky Hill, CT, USA) at 40 rpm for 1 h, and then equilibrated for 30 min before measuring pH and EC with an Extech EC600 pH and digital conductivity meter (Waltham, MA, USA). Measurements of the pH and EC for each biochar were performed in triplicate, and their mean values and standard deviations are reported.

Total carbon (C), nitrogen (N) and hydrogen (H) contents in the biochar samples were analyzed with a CHNO elemental analyzer (Thermo Scientific FLASH 2000 CHNO analyzers, Waltham, MA, USA). Oxygen (O) content was calculated as the weight difference between the raw biochar sample and sum of C, H, and N. The H/C and O/C atomic ratios were subsequently calculated by dividing the mass percentage of each element by its respective atomic weight. Measurements of the elemental compositions for each biochar were performed in triplicate, and their mean values and standard deviation are reported.

Fourier transformation infrared spectroscopy (FT-IR) was used to characterize the surface functional groups of the biochar samples using a PerkinElmer Spectrum Two FT-IR spectrometer (Waltham, MA, USA) equipped with an attenuated total reflection (ATR) accessory. All spectra were acquired by the ATR accessory in the wavenumber range of 650 - 4000 cm^{-1} with 128 scans and a resolution of 4 cm^{-1}. Three replicates were collected for each biochar sample. All the data analyses on the spectra were performed using Spectrum 6 spectroscopy software (PerkinElmer, MA, USA).

X-ray diffraction (XRD) was used to characterize the crystallinity of the biochar samples using a SmartLab X-ray diffractometer (Rigaku Corporation, Tokyo, Japan) with Ni-foil filtered CuKα radiation (wavelength 0.154 nm). The X-ray tube was energized at 40 kV and 30 mA. The samples were scanned from 10° to 80° 2θ using a scan speed of 20.0°·min^{-1}. A compact photon-counting X-ray detector (HyPix-3000) was used to receive the signal. Three replicates were collected for each biochar sample. The crystal phases of components in the biochar samples were determined using the Jade 6 software by comparing the obtained XRD patterns with crystal structure of materials in the database of the International Center for Diffraction Data (ICDD, PDF-2 Release 2005).

The ash content was determined using a Thermogravimetric Analyzer (TGA/DSC 3+, Mettler-Toledo, OH, USA). Approximately 50 mg of ground biochar powder was precisely weighed into a 100 μL alumina crucible. The measurement was conducted under a continuous air flow of 100 mL min^{-1}. The temperature program was executed as follows: the sample was heated from 30 °C to 550 °C at a constant heating rate of 10 °C·min^{-1}, followed by an isothermal hold at 550 °C for 6 h to ensure complete combustion. The mass recorded at 200 °C was used as the dry basis reference point. The ash content was calculated as the percentage of residual mass at the final isothermal stage relative to this dry mass. Ash content was determined in duplicate due to its high measurement reproducibility, and the average values are reported.

2.4. Lead ion adsorption kinetics

Kinetic Adsorption experiments are essential for evaluating the performance of biochar as an “adsorbent”, aiming not only to determine the adsorption capacity but also to elucidate the kinetic characteristics and underlying mechanisms of the adsorption process. In kinetic studies, the time-dependent adsorption experiments were conducted to quantitatively describe the dynamic adsorption behavior of heavy metal ions onto the biochar surface. For the selection of the adsorption kinetics fitting model, the pseudo-second order (PSO) model's flexibility makes it

more robust for multi-mechanism systems, particularly in characterizing chemisorption-dominated processes, whereas the pseudo-first order (PFO) model is limited to simpler, single-mechanism scenarios, which may inadequately represent biochar's chemical adsorption pathways [41,42]. In addition, the PSO model provides a more accurate prediction of the equilibrium adsorption capacity (q_e), which is critical for the objective comparison of the adsorption capabilities of different biochar materials [43].

The biochar Pb(II) adsorption kinetic study for all the biochar samples was performed by adding 100 mg of biochar particles into a 50 mL solution with a Pb(II) concentration of 200 mg L^{-1} in a 50 mL polypropylene centrifuge tube. The tube was then placed onto a Scilogex SciRL-E tube rotator (Rocky Hill, CT, USA) with a rotating speed of 40 rpm at room temperature (22 ± 3 °C). The suspension samples were extracted using syringes and filtered with a 0.45 μm PTFE membrane at 0.17, 0.5, 1, 2, 3, 4, 8, 24, 48, and 72 h. The solutions without biochar were then diluted to measure the Pb(II) concentration using an ultraviolet/visible (UV/Vis) spectrophotometer (UV-1600PC, VWR, Radnor, PA, USA). Quantification of the Pb(II) in aqueous solutions using the UV-Vis measurement followed a published procedure [38].

The Pb(II) adsorption equilibrium capacities of the biochar samples were calculated by fitting the Pb(II) adsorption kinetic data using the PSO model [42]. The linear form of the PSO model shown in equation (1) was used to fit the kinetics data for calculating the Pb(II) adsorption capacity at equilibrium,

$$t / q_t = 1/k_2 q_e^2 + t/q_e \quad (1)$$

where t, q_t, q_e, and k_2 are the time (min), the amount of adsorption of Pb (II) on biochar at any given time t, the amount of adsorption on biochar at equilibrium (adsorption capacity, mg·L^{-1}), and the adsorption rate constant (g·mg^{-1}·min^{-1}), respectively [43,44]. Adsorptions for each biochar were repeated three times, and average values of the adsorption capacities with standard deviation were reported.

2.5. Biochar characterization after Pb(II) adsorption

After the 72-h kinetic study, the Pb(II) biochar mixture solution was allowed to settle for 6-8 h at room conditions to separate the liquid from the solid through sedimentation. The solids in the mixture were collected and then oven-dried at 105 °C for 24 h. The dried solid was then manually ground into powder using a mortar and pestle. FT-IR and XRD analyses were performed on the ground solid samples following identical methodologies described in Section 2.3.

2.6. Statistical analysis

Differences between Elemental composition (C, H, N, and O), pH, EC, surface area, pore volume, and Pb(II) adsorption capacity for all the biochar samples were tested for significance using a one-way analysis of variance (ANOVA, IBM SPSS Statistics 22.0) and Duncan's multiple range tests ($p < 0.05$).

3. Results and discussions

3.1. Biochar characteristics

The C, H, and N contents of the biochar samples are shown in Table 1, and the oxygen (O) content, the O/C and H/C atomic ratios were calculated and also included in Table 1. The elemental composition of biochar is influenced by both the feedstock's elemental composition and pyrolysis temperature [45]. Compared to agricultural and livestock waste, woody biomass is lower in ash and other impurities (e.g., organic extractives), and primarily consists of cellulose, hemicellulose, and lignin (with C, H, N, and O content collectively accounting for 99% of the total elemental composition) [46]. After pyrolysis, all the biochar samples were rich in C (85.70 ± 0.19 - 88.97 ± 3.0 %). Statistical analysis results indicated that there were no significant differences in the C content among different biochar samples. The H content in all the biochar samples ranged from 1.70 ± 0.09 to 1.95 ± 0.06 %, and the statistical analysis showed that red maple and white oak biochar exhibited the highest H contents, with values of 1.95 ± 0.06 and 1.93 ± 0.04 %, respectively, while aspen biochar showed the lowest H contents at 1.70 ± 0.09 %. The O content of the biochar samples was calculated as the difference between biochar mass and the C, H and N contents (O = 100 - C - H - N), and the data ranged from 9.01 ± 3.01 to 12.31 ± 0.18 %, and statistical analysis showed that there was no significant difference among all the biochar samples. The N content ranged from 0.09 ± 0.01 to 0.28 ± 0.08 %. Statistical analysis revealed that chestnut biochar exhibited the highest N content (0.28 ± 0.08 %), while aspen biochar showed the lowest (0.09 ± 0.01%). The atomic ratios H/C and O/C are the primary metrics for evaluating the carbonization, stability, and chemical structural features of biochar. The O/C atomic ratio ranged between 0.08 ± 0.03 and 0.11 ± 0.06, while the H/C atomic ratio fell between 0.232 ± 0.013 and 0.270 ± 0.010. Statistical analysis revealed that there was no significant difference in the O/C atomic ratio among different biochar materials, whereas the H/C atomic ratio showed significant variation. Red maple biochar exhibited the highest H/C atomic ratio, whereas aspen biochar had the lowest. Low H/C (<0.7) and O/C ratios (<0.2) of all the biochar samples indicated they lost more water and O-containing functional groups, and formed more aromatic and stable carbon structures [47,48]. Based on the elemental composition and atomic ratio analysis, it was found that all biochar materials derived from different feedstocks exhibit high carbon content and a high degree of carbonization, reflecting their significant carbon sequestration potential. The consistently low H/C and O/C atomic ratios across all biochar samples indicate that extensive dehydration and

Table 1
Elemental composition of biochar prepared from 12 wood species.

Biochar	N		C	H		O	O/C	H/C	
	%, mass						atomic ratio		
Aspen	0.09 ± 0.01	d	87.96 ± 0.23	1.70 ± 0.09	e	10.25 ± 0.26	0.09 ± 0.01	0.232 ± 0.013	e
Hickory	0.21 ± 0.01	b	85.70 ± 0.19	1.79 ± 0.01	cde	12.31 ± 0.18	0.11 ± 0.01	0.250 ± 0.002	cd
Red maple	0.22 ± 0.04	b	86.72 ± 0.67	1.95 ± 0.06	a	11.11 ± 0.58	0.10 ± 0.01	0.270 ± 0.010	a
White oak	0.20 ± 0.01	bc	86.52 ± 0.90	1.93 ± 0.04	a	11.36 ± 0.90	0.10 ± 0.01	0.267 ± 0.007	ab
Ash	0.16 ± 0.03	bc	88.25 ± 0.54	1.87 ± 0.07	abc	9.71 ± 0.64	0.08 ± 0.01	0.255 ± 0.008	abcd
Yellow poplar	0.15 ± 0.02	bc	87.33 ± 0.56	1.80 ± 0.03	bcd	10.72 ± 0.61	0.09 ± 0.01	0.247 ± 0.002	cd
Black cherry	0.16 ± 0.01	bc	87.79 ± 0.89	1.86 ± 0.03	abc	10.19 ± 0.90	0.09 ± 0.01	0.254 ± 0.002	bcd
Chestnut	0.28 ± 0.08	a	87.89 ± 5.03	1.89 ± 0.01	ab	9.94 ± 5.12	0.09 ± 0.05	0.258 ± 0.014	abcd
Red oak	0.20 ± 0.02	bc	85.91 ± 6.18	1.87 ± 0.04	abc	12.01 ± 6.23	0.11 ± 0.06	0.262 ± 0.014	abc
Birch	0.19 ± 0.05	bc	86.25 ± 4.80	1.77 ± 0.05	de	11.80 ± 4.88	0.10 ± 0.05	0.246 ± 0.010	de
White pine	0.14 ± 0.01	cd	85.92 ± 2.51	1.75 ± 0.05	de	12.19 ± 2.53	0.11 ± 0.03	0.244 ± 0.007	de
Loblolly pine	0.15 ± 0.04	bc	88.97 ± 3.00	1.86 ± 0.04	abc	9.01 ± 3.01	0.08 ± 0.03	0.251 ± 0.003	cd

(Mean values at different experimental conditions followed by the same lowercase letters are not significantly different using Duncan's test at $p < 0.05$.).

decarboxylation reactions occurred during pyrolysis, leading to the formation of highly aromatic and stable carbon structures [47]. Although no significant differences were observed in the carbon content, oxygen content, and O/C atomic ratios among all samples, significant differences were found in nitrogen content, hydrogen content, and H/C ratio, suggesting that the type of feedstock influences certain physical/chemical properties.

The yields of biochar after pyrolysis ranged from 21.56 ± 0.08 to 24.82 ± 0.44 % on a dry-weight basis, as shown in Table 2. Statistical analysis results revealed that there were significant differences in the yields among all biochar samples. Red maple biochar showed the highest yield, whereas aspen had the lowest. The yields of biochar reported here are in a similar range when compared with the literature [49]. All biochar samples in this study were alkaline (pH 7.63-10.05), consistent with the findings of other studies [23,50]. As presented in Table 2, the pH of the biochar prepared from different wood species varied significantly, with aspen biochar showing the highest alkalinity and birch biochar the lowest. During pyrolysis, the organic matrix gradually decomposes with increasing temperature, releasing volatiles and reducing acidic groups, while alkaline minerals are enriched, leading to an increase in pH of the biochar [51]. Under the same preparation processes, the observed variation in biochar pH across different wood species is primarily attributable to differences in the chemical composition of the feedstock, particularly in terms of ash content and its chemical constituents [40].

Ash is the inorganic mineral residue left after the complete combustion of wood. The ash content and its chemical composition vary enormously between wood species [52]. Generally, wood with higher ash content yields biochar with a higher pH value [40]. For instance, hardwood typically contains more ash than softwood [53], which is consistent with the data observed in this study, as presented in Table 2. The ash component of biochar primarily consists of salts, including readily soluble salts, carbonates, sparingly soluble metal oxides and hydroxides, and silicates, the latter being particularly common when the feedstock contains soil particles [40]. The key elements in ash are alkali and alkaline earth metals potassium (K), calcium (Ca), and magnesium (Mg). During pyrolysis, compounds of these elements are converted into corresponding carbonates, oxides, or hydroxides (K_2CO_3, $CaCO_3$, CaO, MgO), which contribute to the alkalinity of the biochar [52,54]. For example, it has been reported that $CaCO_3$ in biochar primarily originates from the thermal conversion of calcium oxalate (CaC_2O_4) present in the wood at temperatures above 400 °C [55]. Among them, K compounds, due to their high solubility, are directly responsible for the elevated initial pH of biochar. Although Ca and Mg compounds have relatively lower solubility, their oxides and carbonates also influence biochar alkalinity. As shown in Table 2, the ash content of the biochar samples ranged from 0.88 ± 0.07 to 2.69 ± 0.02%. White pine biochar exhibited the lowest ash content, whereas hickory biochar showed the highest. In this study, biochar with higher ash content also demonstrated higher pH values. An exception was observed in birch biochar, which had an ash content of 1.12%, higher than that of black cherry, white pine, and loblolly pine biochar samples, but it displayed the lowest pH value and the weakest alkalinity. This could be attributed to the fact that the ash in birch biochar predominantly exists in the form of non-alkaline or weakly alkaline compounds, such as silica [56].

The ash content and its composition also affect the EC of biochar. EC is another critical property of biochar that reflects its soluble salt content and electron transport capabilities [40]. The EC of all biochar samples ranged from 0.20 ± 0.07 to 0.83 ± 0.06 dS m^{-1}. Statistical analysis revealed that aspen, hickory, and red maple biochar exhibited the highest EC, while birch showed the lowest value. This indicates that the ash of aspen, hickory, and red maple biochar is rich in soluble salts; conversely, birch ash contains a lower portion of such soluble components. The observation from the EC measurements is consistent with that from the pH values. Biochar with elevated pH, EC, and ash content demonstrates superior capacity to buffer solution pH, suggesting great potential for Pb(II) removal from acidic solutions [57].

The micropore volumes of the biochar samples, as determined from CO_2 adsorption isotherms using the D-A equation and summarized in Table 2, ranged between 0.16 ± 0.01 to 0.17 ± 0.01 cm^3 g^{-1}. Based on these micropore volumes, the SSA were further derived, yielding values from 417 ± 14 to 436 ± 29 m^2 g^{-1} (Table 2). The D-A equation allows for the direct calculation of micropore volume based on CO_2 adsorption data, which subsequently enables the estimation of the micropore-specific surface area [37]. These values are consistent with and on the higher end of those reported in other studies, which indicates that the porous structure of the woody biochar was well-developed under the preparation conditions of this study [58], suggesting significant potential for the adsorption of small molecular contaminants. However, statistical analysis indicated no significant differences in either SSA or micropore volume among the 12 biochar samples derived from different wood feedstocks with different vessel cell structures ($p > 0.05$).

The FT-IR spectra of the biochar samples were measured to characterize the surface functional groups, and the spectra of all 12 biochar samples are shown in Fig. 1. Identification of functional groups was achieved by comparing characteristic absorption peaks against reference spectra from the literature, and the peak assignments are summarized in Table 3. Peak #1, located in the region between 1695 and 1691 cm^{-1}, is attributed to the C=O vibration in the carboxylic group [38,59,60]. Peak #2 is identified as carboxylate anion (COO^-) vibration at around 1563 cm^{-1} [59]. Peak #3 at 1400 cm^{-1} can be assigned to carbonate derived from inorganic ash often associated with biochar [59]. Peak 3 was observed in aspen and hickory biochar samples, indicated by dashed lines, while absent in all others. The weak signals at

Table 2
Physical and chemical properties of biochar samples.

Biochar	Yield		pH		EC ($dS \cdot m^{-1}$)		Ash content (%)	Dubinin-Astakhov for CO_2 adsorption	
	%, mass							Micropore SSA ($m^2 \cdot g^{-1}$)	Micropore volume ($cm^3 \cdot g^{-1}$)
Aspen	21.56 ± 0.08	f	10.05 ± 0.01	a	0.78 ± 0.12	a	2.06 ± 0.15	417 ± 14	0.16 ± 0.01
Hickory	24.13 ± 0.54	abc	10.04 ± 0.08	ab	0.83 ± 0.06	a	2.69 ± 0.02	436 ± 29	0.16 ± 0.01
Red maple	24.82 ± 0.44	a	9.97 ± 0.02	ab	0.80 ± 0.03	a	1.68 ± 0.01	423 ± 14	0.16 ± 0.01
White oak	24.06 ± 0.08	abc	9.96 ± 0.05	ab	0.49 ± 0.02	b	1.99 ± 0.03	425 ± 21	0.16 ± 0.01
Ash	23.49 ± 0.48	cd	9.37 ± 0.03	d	0.33 ± 0.01	cd	1.37 ± 0.07	437 ± 13	0.16 ± 0.01
Yellow poplar	22.21 ± 0.56	ef	9.33 ± 0.04	d	0.44 ± 0.01	b	1.50 ± 0.01	434 ± 14	0.16 ± 0.01
Black cherry	23.64 ± 0.40	bcd	9.00 ± 0.14	e	0.33 ± 0.13	cd	1.02[a]	429 ± 21	0.16 ± 0.01
Chestnut	24.15 ± 0.09	abc	9.61 ± 0.02	c	0.28 ± 0.01	de	1.24 ± 0.04	434 ± 13	0.16 ± 0.01
Red oak	24.68 ± 0.43	ab	9.92 ± 0.02	b	0.50 ± 0.02	b	2.04 ± 0.01	425 ± 17	0.16 ± 0.01
Birch	22.84 ± 0.15	de	7.63 ± 0.12	g	0.20 ± 0.07	e	1.12 ± 0.06	437 ± 16	0.17 ± 0.01
White pine	24.61 ± 1.50	ab	8.28 ± 0.05	f	0.30 ± 0.03	de	0.88 ± 0.07	430 ± 13	0.16 ± 0.01
Loblolly pine	24.65 ± 0.50	ab	9.10 ± 0.03	e	0.41 ± 0.04	bc	0.90 ± 0.01	427 ± 17	0.16 ± 0.01

(Mean values at different experimental conditions followed by the same lowercase letters are not significantly different using Duncan's test at $p < 0.05$.).
[a] All values in this group were identical (SD = 0).

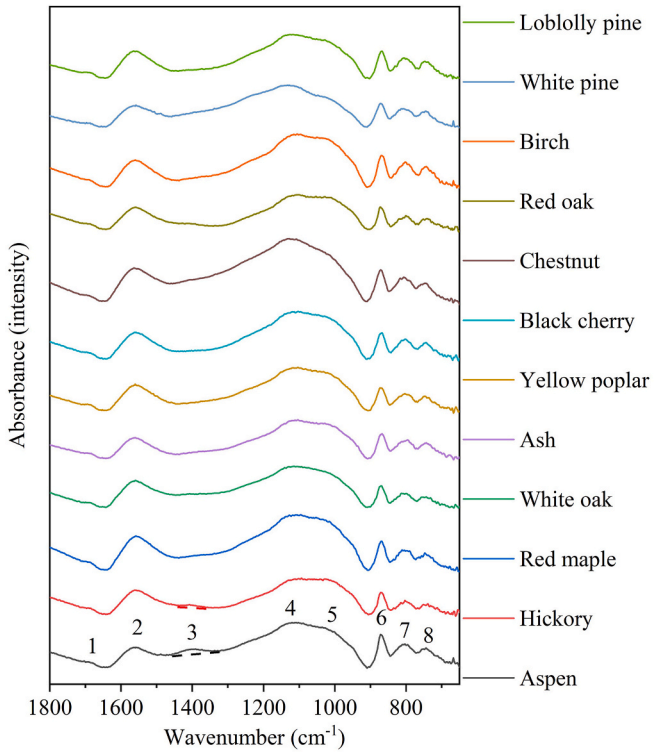

Fig. 1. The FT-IR spectra of 12 woody biochar samples.

Table 3
The surface functional groups of biochar samples characterized by FT-IR.

PeakNo.	Wavenumber (cm^{-1})	Peak assignments
1	1692	C=O from carboxylic acids, amides, esters and ketones
2	1563	COO^- carboxylate anions
3	1400	Carbonate
4, 5	1103, 1020	C-O
6,7,8	871, 810, 744	Aromatic C-H bond

peaks 4 (1103 cm^{-1}) and 5 (1020 cm^{-1}) are ascribed to C-O stretching vibrations in thermally stable oxygen-containing functional groups (e.g., esters, ethers) embedded within the aromatic carbon matrix [59,61]. The aromatic character of the biochar was further evidenced by C-H bending peaks (peaks 6, 7, and 8) from aromatic units condensed into larger sheets during pyrolysis [38,61]. Except for the carbonate peak (peak #3), all 12 woody biochar samples exhibited similar characteristic peaks.

X-ray diffraction (XRD) is a technique for the analysis of the crystalline structure of components in biochar by measuring diffraction patterns and comparing them to standard reference patterns in the Joint Committee on Powder Diffraction Standards (JCPDS) database. XRD analysis was carried out to identify the crystalline structure of the components in the biochar samples, with results presented in Fig. 2. All biochar samples exhibited relatively broad and diffuse diffraction peaks within the 2θ ranges of 18-27° and 40-50°. In the XRD patterns, these characteristic peaks correspond to the C (002) and C (100) planes, indicative of amorphous carbon structures [62,63]. A sharp peak was detected at $2\theta = 29.5°$ in aspen, hickory, white oak, and red oak biochar samples, which corresponds to calcite ($CaCO_3$) in biochar [64,65]. In comparison, there are no such sharp diffraction peaks at $2\theta = 29.5°$ in other biochar samples, indicating that there are no or a non-detectable amount of inorganic substances in the biochar samples from these wood species.

3.2. Pb(II) sorption

Biochar samples were evaluated for their ability to adsorb Pb(II) in aqueous solutions. The Pb(II) adsorption capacities for all the biochar sample were determined and the results are presented in Fig. 3a. At the initial Pb(II) concentration of 200 mg L^{-1}, the Pb(II) adsorption capacities of biochar samples ranged from 12.2 ± 1.1 to 42.7 ± 0.4 mg g^{-1}. Statistical analysis indicated significant differences in Pb(II) adsorption capacities among biochar samples derived from different wood species. In this study, hardwood biochar samples exhibited significantly greater Pb(II) adsorption capacity than that of softwood biochar samples (white pine and loblolly pine biochar), with aspen biochar demonstrating the highest adsorption capacity of 42.7 mg g^{-1}, which was 3.5 times higher than that of loblolly pine biochar (12.2 mg g^{-1}) (Fig. 3a). Among different species of hardwoods, the biochar also showed different Pb(II) adsorption capacities. The Pb(II) adsorption behaviors are significantly impacted by the wood species of the forest feedstocks. Aspen biochar, which exhibited relatively high pH, EC, ash content, and distinct carbonate peaks in the FT-IR spectrum along with the characteristic $CaCO_3$ peaks in XRD compared with other biochar samples, demonstrated the highest lead ion removal capacity, highlighting the significant influence of biochar's physicochemical properties on adsorption performance. The physicochemical characterization indicated that hardwood raw materials and biochars have relatively higher $CaCO_3$ compared with softwood. For manufacturing biochar from wood, attention needs to be paid to the raw materials to ensure the consistent performance of the biochar in Pb(II) adsorption applications. The linear form of the PSO model was

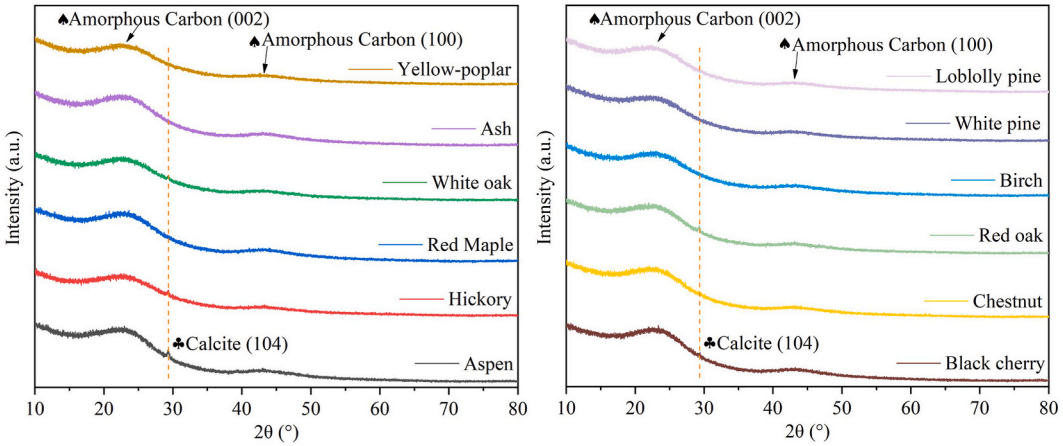

Fig. 2. XRD patterns of 12 woody biochar samples.

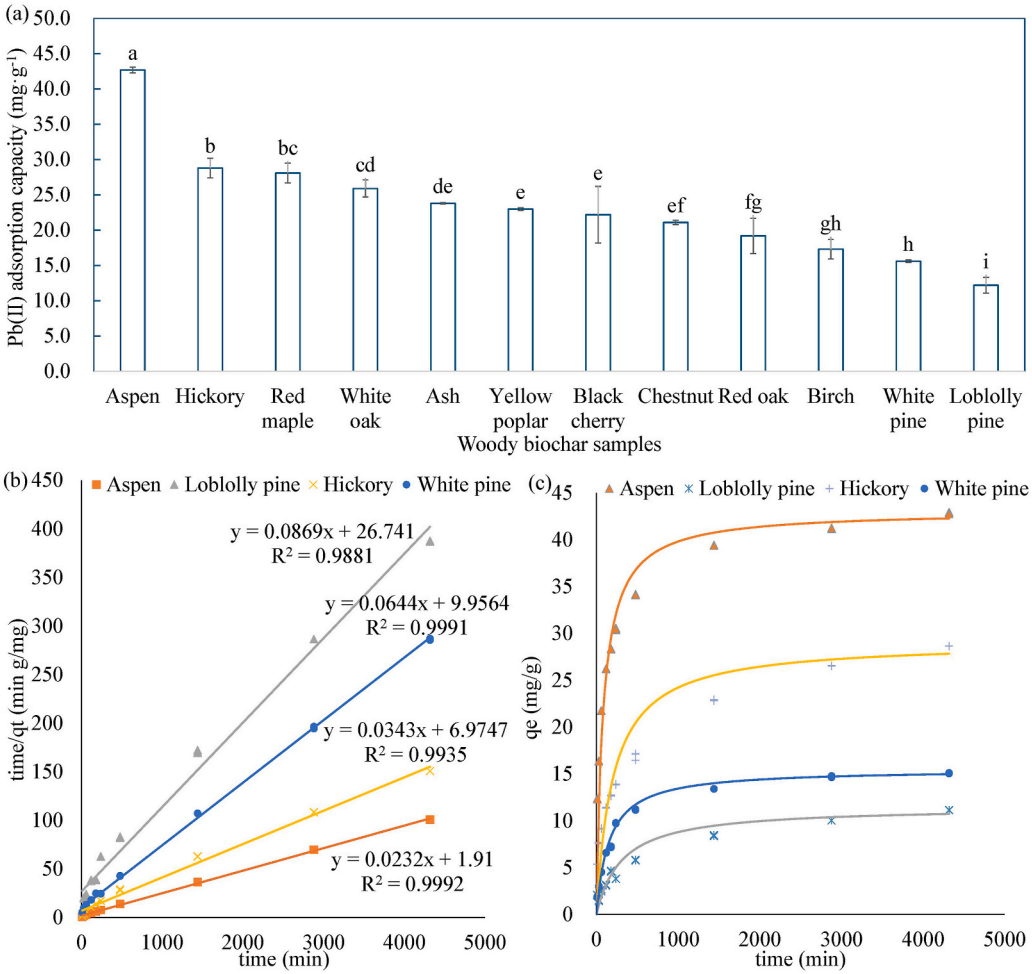

Fig. 3. (a) Pb(II) adsorption capacities of all the biochar samples (Error bars represent standard deviations.), (b) the PSO linear form for the kinetic study of the Pb(II) adsorption by the biochar samples of Aspen, Hickory, White pine and Loblolly pine, and (c) the adsorption kinetics of biochar samples of Aspen, Hickory, White pine and Loblolly pine on Pb(II).

applied by plotting time/*qt* versus time as shown in equation (1). The kinetic data were fitted with the linearized forms of the PSO model, and the values of the correlation coefficients (R^2) are presented in Fig. 3b. The nonlinear forms of the kinetic models were also checked to eliminate the inherent limitations of linearization [66]. As presented in Fig. 3c, the nonlinear fitting curve of the PSO model aligns well with the experimental data points. Therefore, the adsorption process can be well-described by the PSO kinetic model. The PSO model assumes that the rate-limiting step in the adsorption process is the chemical sorption reaction between the adsorbate and the adsorbent [67], which indicates that the Pb(II) adsorption involves chemical interactions between biochar components and Pb(II).

3.3. Biochar characterization after Pb(II) adsorption

Comparative analysis of FT-IR spectra for biochar before and after Pb (II) adsorption experiments was done to investigate reaction mechanisms through changes in surface functional groups on biochar. Consequently, aspen and loblolly pine biochar were selected for contrasting assessment since they showed the highest and lowest Pb(II) adsorption capacities among 12 woody biochar samples. Their FT-IR spectra before and after lead adsorption are presented in Fig. 4. The figure reveals that the FT-IR spectrum of aspen biochar after Pb(II) adsorption shows no significant shift or emergence of different characteristic peaks compared to pristine biochar. In contrast, loblolly pine biochar exhibits a distinct new peak at position 3 after adsorption. The peak 3 corresponds to

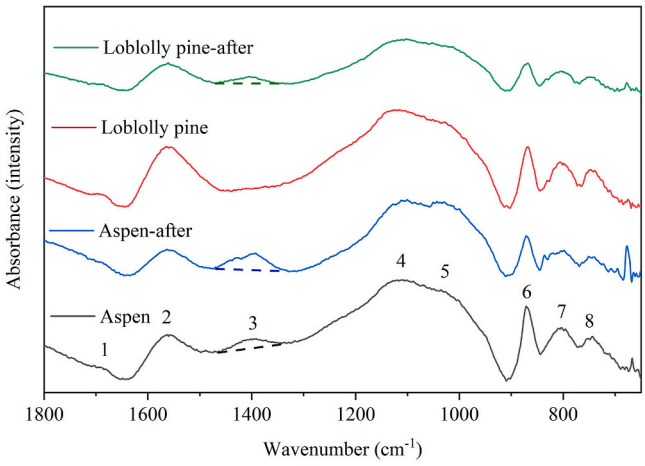

Fig. 4. The FT-IR spectra of biochar samples after Pb(II) adsorption.

carbonate, suggesting potential formation of lead carbonate ($PbCO_3$) precipitates during the Pb(II) adsorption process [68].

Comparative XRD analysis before and after Pb(II) adsorption elucidates reaction mechanisms through crystalline phase transformations in biochar. Fig. 5 presents the XRD patterns of aspen and loblolly pine biochar before and after adsorption. The XRD pattern of pristine aspen

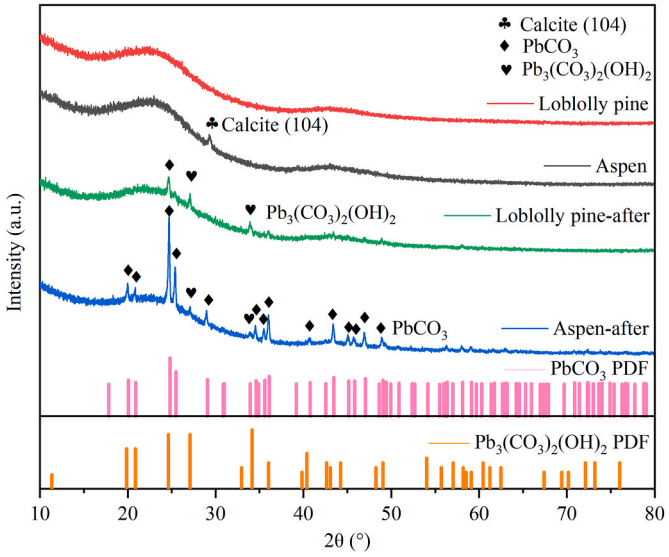

Fig. 5. XRD patterns of biochar samples after Pb(II) adsorption.

biochar exhibited distinct calcite (104) ($CaCO_3$) characteristic peaks. Post-adsorption analysis of aspen revealed the disappearance of these $CaCO_3$ peaks with the concomitant emergence of new crystalline phases, cerussite ($PbCO_3$) and hydrocerussite [$Pb_3(CO_3)_2(OH)_2$]. The peaks at 20.06°, 20.90°, 24.80°, 25.49°, 29.09°, 34.60°, 35.59°, 36.13°, 40.78°, 43.47°, 45.16°, 45.81°, 47.04°, 48.63° show the presence of crystalline structure of $PbCO_3$. The peaks at 27.17° and 34.07° indicate the crystalline phase of $Pb_3(CO_3)_2(OH)_2$. Based on the peak intensity of aspen biochar after Pb(II) adsorption, $PbCO_3$ constituted the dominant crystalline phase, with $Pb_3(CO_3)_2(OH)_2$ as the minor component [69]. The XRD pattern of pristine loblolly pine biochar exhibited two broad diffraction peaks characteristic of amorphous carbon (002 and 100 plane), with no detectable crystalline phases of $CaCO_3$. After Pb(II) adsorption, distinct peaks emerged at 27.17° and 34.07° assigned to $Pb_3(CO_3)_2(OH)_2$, alongside a $PbCO_3$ peak at 24.80°. Peak intensity analysis confirmed $Pb_3(CO_3)_2(OH)_2$ and $PbCO_3$ are the dominant crystalline phases of loblolly pine biochar after Pb(II) adsorption. This is likely because the $CaCO_3$ content in the loblolly pine biochar was too low to be detected by XRD, or the crystallinity of the soluble carbonate salts in its ash was not sufficiently high for XRD detection. However, due to the low solubility product (Ksp) of $Pb_3(CO_3)_2(OH)_2$ and $PbCO_3$, the loblolly pine biochar could still supply a sufficient amount of carbonate ions to precipitate Pb(II). Additionally, carbon dioxide (CO_2) in the air can also dissolve in trace amounts in the solution to form carbonate ions. Furthermore, apart from the biochar reported in Fig. 5, all other biochar samples exhibited characteristic $Pb_3(CO_3)_2(OH)_2$ and $PbCO_3$ peaks in their XRD patterns after Pb(II) adsorption experiments. The observation demonstrated that precipitation of $PbCO_3$ and $Pb_3(CO_3)_2(OH)_2$ constitutes a primary mechanism for aqueous Pb(II) adsorption by biochar [68]. Consistent with other studies, the presence of ash components in the biochar, particularly $CaCO_3$, was reported to significantly facilitate heavy metal removal by biochar through precipitation mechanisms [68, 70,71].

In addition, the significantly higher intensity of the Pb(II)-based carbonate crystalline peaks ($PbCO_3$, and $Pb_3(CO_3)_2(OH)_2$) in the aspen biochar compared to those in the loblolly pine sample suggests a greater extent of Pb(II)-based carbonate precipitation and, consequently, higher adsorption capacity. This difference is further supported by the higher ratio of crystalline Pb(II)-based carbonate mineral peak intensities to the broad signal from amorphous carbon in aspen biochar, indicating more pronounced precipitate formation following Pb(II) uptake.

The morphology and elemental proportions of the aspen and loblolly pine biochar materials before and after Pb(II) adsorption were determined using the SEM-EDX technique (Fig. 6). The representative SEM images (1a-4a) show the overall surface morphology, while the (1 b-4b) show magnified view of the region indicated by the red square in (a), allowing closer observation of the surface texture. The corresponding EDX analyses of (1c-4c) identify the elemental species present of the red square in (b), which are essential for understanding the potential adsorption mechanisms. For the aspen biochar prior to adsorption (Figs. 6–1 b), the EDX analysis revealed the presence of Ca along with C and O. In combination with the XRD pattern, these features suggest the existence of $CaCO_3$ on the biochar surface. After Pb(II) adsorption (Figs. 6–2 b), the surface became extensively covered with Pb-containing precipitates, while Ca was no longer detected by EDX. This indicates that $CaCO_3$ played a key role in lead removal, likely via dissolution and subsequent precipitation of lead as $PbCO_3$ or $Pb_3(CO_3)_2(OH)_2$, accompanied by the release of Ca (II) into solution. In contrast, for loblolly pine biochar, which exhibited the lowest adsorption capacity, no distinct Ca-rich phases were observed on the pristine surface (Figs. 6–3 b). After lead exposure (Figs. 6–4 b), only sparse Pb-containing precipitates were detected, consistent with its limited adsorption performance. These results suggest that the presence of $CaCO_3$ is a decisive factor governing the lead removal efficiency of the biochar materials.

The characterization of the physicochemical properties of 12 biochar samples revealed that all biochar samples produced in this study under the given experimental conditions exhibited high aromaticity, stable carbon structures, and well-developed microporosity. No significant differences were found in the micropore surface area and micropore volume of biochars derived from wood feedstocks with different vessel cell structures. However, the different wood feedstocks resulted in significant variations in elemental composition (N and H), yield, ash content, pH, and EC. These differences in physicochemical properties led to varying performances in the adsorption of heavy metal Pb(II) from aqueous solution.

This study found that biochar with elevated pH, EC, and ash content demonstrated high adsorption capacity for Pb(II) removal from solution. This is likely because ash content influences both pH and EC. The readily soluble salts in the ash can buffer the solution pH and increase EC during dissolution. Sufficient ash content can adjust the pH of the metal ion solution to neutral or weakly alkaline, promoting the transformation of metal ions into more stable precipitated forms. Furthermore, $CaCO_3$ present in the ash of biochar can provide carbonate ions, leading to the formation of Pb-based carbonate precipitates ($PbCO_3$, and $Pb_3(CO_3)_2(OH)_2$).

Additionally, the 12 types of wood-derived biochar samples showed similar microporous specific surface area and micropore volume, indicating that the differences in Pb(II) adsorption capacity were not mainly caused by the pore structure, but were dominantly determined by variations in ash content and composition, particularly the content of soluble carbonate salts and $CaCO_3$ in the biochar.

4. Conclusions

This study investigated the influence of wood species on the physicochemical properties of biochar and its Pb(II) adsorption capacities. Twelve biochar samples derived from different wood feedstocks were produced under identical pyrolysis conditions and systematically characterized in terms of elemental composition, pH, EC, SSA, pore volume, surface functional groups, morphology (SEM-EDX), and crystalline structures. To elucidate the adsorption mechanism, biochar samples were also characterized after Pb(II) exposure. The results indicated that the Pb(II) removal capacity of biochars derived from hardwoods was significantly higher than that of softwood-derived biochars. Under the same pyrolysis conditions, wood feedstocks with varying vessel structures did not significantly affect the microporous structure of the resulting biochars. However, marked differences were observed in pH, EC, and Pb(II) adsorption capacity. The variation in the Pb(II)

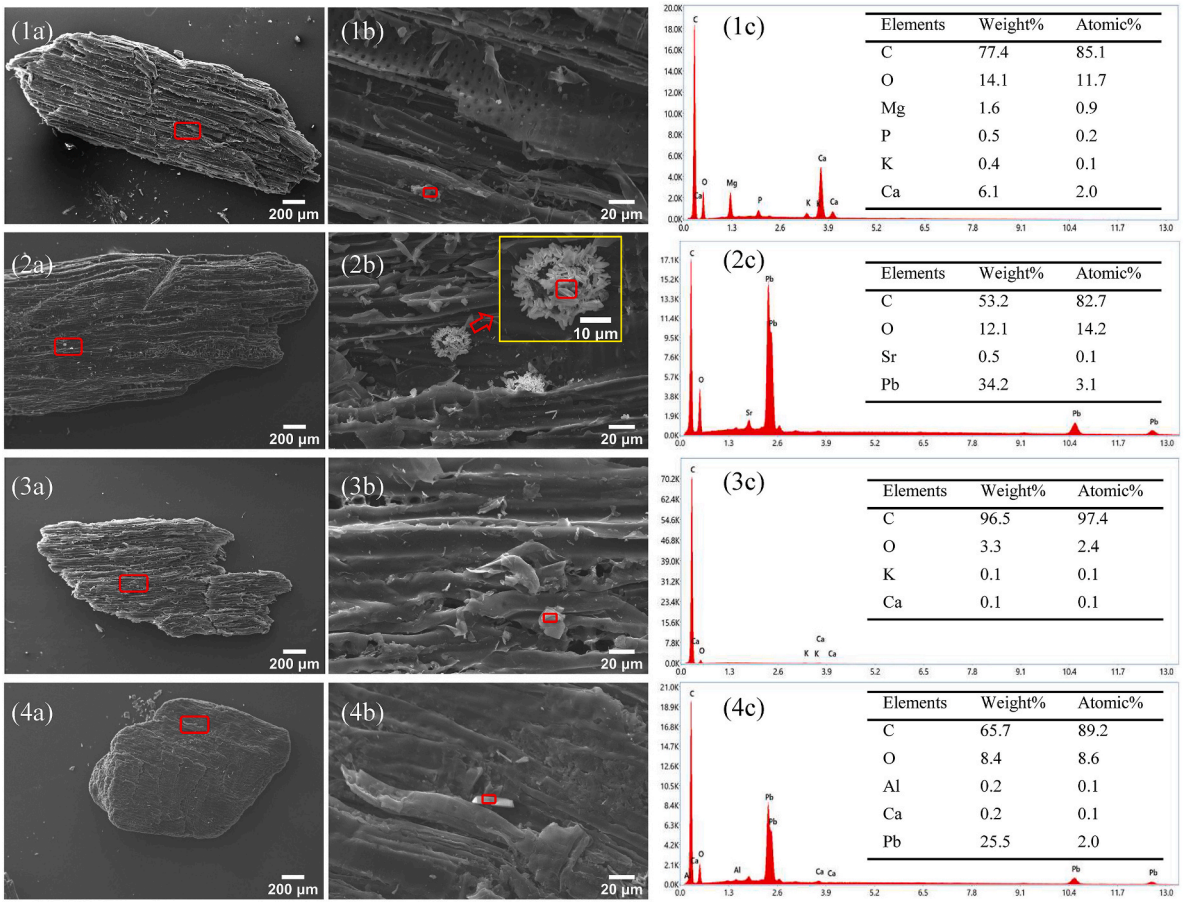

Fig. 6. SEM images of biochar samples before and after Pb(II) adsorption. (a) SEM image of the biochar; (b) higher magnification of the region indicated by the red square in (a); (c) EDX spectrum acquired from the red square area in (b). 1. Aspen biochar before Pb(II) adsorption. 2. Aspen biochar after Pb(II) adsorption. 3. Loblolly pine biochar before Pb(II) adsorption. 4. Loblolly pine biochar after Pb(II) adsorption.

adsorption performance was primarily governed by the ash content and composition, particularly the presence of soluble salts and $CaCO_3$. The primary mechanisms of Pb(II) removal by biochar involved solution pH buffering mediated by soluble salts, followed by precipitation of $PbCO_3$, and $Pb_3(CO_3)_2(OH)_2$ through the reaction between $CaCO_3$ and Pb(II). These findings provide valuable insights for the feedstock selection and development of biochar materials with enhanced adsorption performance.

CRediT authorship contribution statement

Ruiqi Li: Conceptualization, Formal analysis, Investigation, Methodology, Writing – original draft. **Tara Keyser:** Resources, Writing – review & editing. **Thomas Elder:** Conceptualization, Methodology, Resources, Supervision, Writing – review & editing. **Qiangu Yan:** Resources, Writing – review & editing. **Zhiyong Cai:** Resources, Writing – review & editing. **Yucheng Peng:** Conceptualization, Funding acquisition, Methodology, Resources, Supervision, Writing – review & editing.

Declaration of competing interest

The authors declare that they have no known competing financial interests or personal relationships that could have appeared to influence the work reported in this paper.

Acknowledgements

Authors thank financial support from the U.S. Endowment for Forestry & Communities [grant no. G00016056]; USDA Forest Service [grant no. 24-JV11330101-004]; Southern Research Station [grant no. 23-JV-11330170-064].

Data availability

Data will be made available on request.

References

[1] S. Anubhav, S. Anuj, K.V. Rohit, L.C. Rushikesh, P.P. Pritam, N. Varad, A. Vinay, K. C. Sumit, A. Garima, K.A. Kumud, S.S. Mahipal, Heavy metal contamination of water and their toxic effect on living organisms, in: D. Daniel Junqueira, O. Danielle Palma de (Eds.), The Toxicity of Environmental Pollutants, IntechOpen, Rijeka, 2022. Ch. 2.
[2] R. Reza, G. Singh, Heavy metal contamination and its indexing approach for river water, Int. J. Environ. Sci. Technol. 7 (2010) 785–792.
[3] J. Briffa, E. Sinagra, R. Blundell, Heavy metal pollution in the environment and their toxicological effects on humans, Heliyon 6 (9) (2020).
[4] A.K. Tiwari, M. De Maio, P.K. Singh, M.K. Mahato, Evaluation of surface water quality by using GIS and a heavy metal pollution index (HPI) model in a coal mining area, India, Bull. Environ. Contam. Toxicol. 95 (2015) 304–310.
[5] Q. Zhou, N. Yang, Y. Li, B. Ren, X. Ding, H. Bian, X. Yao, Total concentrations and sources of heavy metal pollution in global river and Lake water bodies from 1972 to 2017, Glob. Ecol. Conserv. 22 (2020) e00925.
[6] H. Ali, E. Khan, What are heavy metals? long-Standing controversy over the scientific use of the term 'heavy metals' – proposal of a comprehensive definition, Toxicol. Environ. Chem. 100 (1) (2018) 6–19.
[7] K.F. Kayani, S.J. Mohammed, Heavy metal pollution in aquatic environments and removal using highly efficient bimetallic metal–organic framework adsorbents, RSC Adv. 15 (43) (2025) 35756–35769.
[8] K.F. Kayani, S.J. Mohammed, Mercury in aquatic environments: toxicity and advances in remediation using covalent organic frameworks, Mater. Adv. 6 (11) (2025) 3371–3385.

[9] J. Namieśnik, A. Rabajczyk, The speciation and physico-chemical forms of metals in surface waters and sediments, Chem. Speciat. Bioavailab. 22 (1) (2010) 1–24.
[10] B. Simon-Hettich, A. Wibbertmann, D. Wagner, L. Tomaska, H. Malcolm, Environmental Health Criteria 221: Zinc, 2001.
[11] S.H. Badawy, M.I.D. Helal, A.M. Chaudri, K. Lawlor, S.P. McGrath, Soil solid-phase controls lead activity in soil solution, J. Environ. Qual. 31 (1) (2002) 162–167.
[12] R. Świetlik, Speciation analysis of chromium in waters, Pol. J. Environ. Stud. 7 (5) (1998) 257–266.
[13] A.S. Mohammed, A. Kapri, R. Goel, Heavy metal pollution: source, impact, and remedies, in: M.S. Khan, A. Zaidi, R. Goel, J. Musarrat (Eds.), Biomanagement of Metal-Contaminated Soils, Springer, Netherlands: Dordrecht, 2011, pp. 1–28.
[14] Z. Wang, P. Luo, X. Zha, C. Xu, S. Kang, M. Zhou, D. Nover, Y. Wang, Overview assessment of risk evaluation and treatment technologies for heavy metal pollution of water and soil, J. Clean. Prod. 379 (2022) 134043.
[15] M. Kumar, M. Nandi, K. Pakshirajan, Recent advances in heavy metal recovery from wastewater by biogenic sulfide precipitation, J. Environ. Manag. 278 (2021) 111555.
[16] A. Dąbrowski, Z. Hubicki, P. Podkościelny, E. Robens, Selective removal of the heavy metal ions from waters and industrial wastewaters by ion-exchange method, Chemosphere 56 (2) (2004) 91–106.
[17] A.E. Lewis, Review of metal sulphide precipitation, Hydrometallurgy 104 (2) (2010) 222–234.
[18] F. Fu, Q. Wang, Removal of heavy metal ions from wastewaters: a review, J. Environ. Manag. 92 (3) (2011) 407–418.
[19] B. Qiu, X. Tao, H. Wang, W. Li, X. Ding, H. Chu, Biochar as a low-cost adsorbent for aqueous heavy metal removal: a review, J. Anal. Appl. Pyrolysis 155 (2021) 105081.
[20] S. Mansoor, N. Kour, S. Manhas, S. Zahid, O.A. Wani, V. Sharma, L. Wijaya, M. N. Alyemeni, A.A. Alsahli, H.A. El-Serehy, B.A. Paray, P. Ahmad, Biochar as a tool for effective management of drought and heavy metal toxicity, Chemosphere 271 (2021) 129458.
[21] X.-f. Tan, S.-b. Liu, Y.-g. Liu, Y.-l. Gu, G.-m. Zeng, X.-j. Hu, X. Wang, S.-h. Liu, L.-h. Jiang, Biochar as potential sustainable precursors for activated carbon production: multiple applications in environmental protection and energy storage, Bioresour. Technol. 227 (2017) 359–372.
[22] C. Wang, X. Wang, N. Li, J. Tao, B. Yan, X. Cui, G. Chen, Adsorption of lead from aqueous solution by biochar: a review, Cleanroom Technol. 4 (3) (2022) 629–652.
[23] Q. Ye, L. Qianhui, X. Li, Removal of heavy metals from wastewater using biochars: adsorption and mechanisms, Environ. Pollut. Bioavailab. 34 (1) (2022) 385–394.
[24] G. Lin, Y. Wang, X. Wu, J. Meng, Y.S. Ok, C.-H. Wang, Enhancing agricultural productivity with biochar: evaluating feedstock and quality standards, Bioresour. Technol. Rep. 29 (2025) 102059.
[25] J. Chen, J. Zhou, W. Zheng, S. Leng, Z. Ai, W. Zhang, Z. Yang, J. Yang, Z. Xu, J. Cao, M. Zhang, L. Leng, H. Li, A complete review on the oxygen-containing functional groups of biochar: formation mechanisms, detection methods, engineering, and applications, Sci. Total Environ. 946 (2024) 174081.
[26] C.L. Williams, R.M. Emerson, J.S. Tumuluru, Biomass compositional analysis for conversion to renewable fuels and chemicals, Biomass volume estimation and valorization for energy (2017) 251–270.
[27] M. Danish, T. Ahmad, A review on utilization of wood biomass as a sustainable precursor for activated carbon production and application, Renew. Sustain. Energy Rev. 87 (2018) 1–21.
[28] T. Zhang, J. Huang, S. Deng, G. Yu, Influence of pesticides contamination on the emission of PCDD/PCDF to the land from open burning of corn straws, Environmental Pollution 159 (6) (2011) 1744–1748.
[29] K. Szymański, B. Janowska, P. Jastrzębski, Heavy metal compounds in wastewater and sewage sludge, Rocznik Ochrona Środowiska 13 (2011) 83–99.
[30] M. Askeland, B. Clarke, J. Paz-Ferreiro, Comparative characterization of biochars produced at three selected pyrolysis temperatures from common woody and herbaceous waste streams, PeerJ 7 (2019) e6784.
[31] L. Wang, M.N.P. Olsen, C. Moni, A. Dieguez-Alonso, J.M. de la Rosa, M. Stenrød, X. Liu, L. Mao, Comparison of properties of biochar produced from different types of lignocellulosic biomass by slow pyrolysis at 600 °C, Applications in Energy and Combustion Science 12 (2022) 100090.
[32] K. Intani, S. Latif, Z. Cao, J. Müller, Characterisation of biochar from maize residues produced in a self-purging pyrolysis reactor, Bioresour. Technol. 265 (2018) 224–235.
[33] N. Tripathi, C.D. Hills, R.S. Singh, C.J. Atkinson, Biomass waste utilisation in low-carbon products: harnessing a major potential resource, npj Clim. Atmos. Sci. 2 (1) (2019) 35.
[34] J.P. Prestemon, T.P. Holmes, J. Pye, H. Rauscher, Y. Sands, D. Lee, J. Beatty, Economic impacts of hurricanes on forest owners, Pye, John M; Rauscher, H Michael; Sands, Yasmeen; Lee, Danny C (2010) 207–221.
[35] S.G. McNulty, Hurricane impacts on US forest carbon sequestration, Environmental Pollution 116 (2002) S17–S24.
[36] Z. Shen, Y. Zhang, F. Jin, O. McMillan, A. Al-Tabbaa, Qualitative and quantitative characterisation of adsorption mechanisms of lead on four biochars, Sci. Total Environ. 609 (2017) 1401–1410.
[37] A.P. Terzyk, P.A. Gauden, P. Kowalczyk, What kind of pore size distribution is assumed in the dubinin–astakhov adsorption isotherm equation? Carbon 40 (15) (2002) 2879–2886.
[38] Y. Peng, R. Li, M. Irfan, S. Liu, D. Wang, T. Elder, Q. Yan, Z. Cai, Lead ion adsorption by biochar manufactured from downed timber: the effect of downed timber maturity and environmental exposure period, Wood Mater. Sci. Eng. (2024) 1–12.
[39] K.C. Kim, T.-U. Yoon, Y.-S. Bae, Applicability of using CO2 adsorption isotherms to determine BET surface areas of microporous materials, Microporous Mesoporous Mater. 224 (2016) 294–301.
[40] B. Singh, M.M. Dolk, Q. Shen, M. Camps-Arbestain, Biochar pH, electrical conductivity and liming potential, Biochar: A guide to analytical methods 23 (2017).
[41] S.S. Mayakaduwa, P. Kumarathilaka, I. Herath, M. Ahmad, M. Al-Wabel, Y.S. Ok, A. Usman, A. Abduljabbar, M. Vithanage, Equilibrium and kinetic mechanisms of woody biochar on aqueous glyphosate removal, Chemosphere 144 (2016) 2516–2521.
[42] J. Wang, X. Guo, Adsorption kinetic models: physical meanings, applications, and solving methods, J. Hazard Mater. 390 (2020) 122156.
[43] Y.S. Ho, G. McKay, Pseudo-second order model for sorption processes, Process Biochemistry 34 (5) (1999) 451–465.
[44] E.D. Revellame, D.L. Fortela, W. Sharp, R. Hernandez, M.E. Zappi, Adsorption kinetic modeling using pseudo-first order and pseudo-second order rate laws: a review, Clean. Eng. Technol. 1 (2020) 100032.
[45] S. Wang, B. Gao, A.R. Zimmerman, Y. Li, L. Ma, W.G. Harris, K.W. Migliaccio, Physicochemical and sorptive properties of biochars derived from woody and herbaceous biomass, Chemosphere 134 (2015) 257–262.
[46] R.C. Pettersen, The chemical composition of wood, The chemistry of solid wood 207 (1984) 57–126.
[47] L. Leng, H. Huang, H. Li, J. Li, W. Zhou, Biochar stability assessment methods: a review, Sci. Total Environ. 647 (2019) 210–222.
[48] K.A. Spokas, Review of the stability of biochar in soils: predictability of O: c molar ratios, Carbon Manag. 1 (2) (2010) 289–303.
[49] M. Tripathi, J.N. Sahu, P. Ganesan, Effect of process parameters on production of biochar from biomass waste through pyrolysis: a review, Renew. Sustain. Energy Rev. 55 (2016) 467–481.
[50] A. Tomczyk, Z. Sokołowska, P. Boguta, Biochar physicochemical properties: pyrolysis temperature and feedstock kind effects, Rev. Environ. Sci. Biotechnol. 19 (1) (2020) 191–215.
[51] M. García-Jaramillo, L. Cox, H.E. Knicker, J. Cornejo, K.A. Spokas, M.C. Hermosín, Characterization and selection of biochar for an efficient retention of tricyclazole in a flooded alluvial paddy soil, J. Hazard Mater. 286 (2015) 581–588.
[52] J. Werkelin, B.-J. Skrifvars, M. Hupa, Ash-forming elements in four Scandinavian wood species. Part 1: summer harvest, Biomass Bioenergy 29 (6) (2005) 451–466.
[53] F.N.D. Mukome, X. Zhang, L.C.R. Silva, J. Six, S.J. Parikh, Use of chemical and physical characteristics to investigate trends in biochar feedstocks, J. Agric. Food Chem. 61 (9) (2013) 2196–2204.
[54] L. Etiégni, A.G. Campbell, Physical and chemical characteristics of wood ash, Bioresour. Technol. 37 (2) (1991) 173–178.
[55] F. Rees, F. Watteau, S. Mathieu, M.-P. Turpault, Y. Le Brech, R. Qiu, J.L. Morel, Metal immobilization on wood-derived biochars: distribution and reactivity of carbonate phases, J. Environ. Qual. 46 (4) (2017) 845–854.
[56] A.F. Boss, F.L. Braghiroli, G. Amaral-Labat, A.A. Souza, M.R. Baldan, H. Bouafif, A. Koubaa, G.F. Lenz e Silva, Dielectric characterization of white birch–activated biochar composites: a sustainable alternative to radar-absorbing materials, J. Compos. Mater. 54 (9) (2020) 1233–1244.
[57] J. Komkiene, E. Baltrenaite, Biochar as adsorbent for removal of heavy metal ions [Cadmium(II), Copper(II), Lead(II), Zinc(II)] from aqueous phase, Int. J. Environ. Sci. Technol. 13 (2) (2016) 471–482.
[58] L. Leng, Q. Xiong, L. Yang, H. Li, Y. Zhou, W. Zhang, S. Jiang, H. Li, H. Huang, An overview on engineering the surface area and porosity of biochar, Sci. Total Environ. 763 (2021) 144204.
[59] C.T. Johnston, 18 biochar analysis by fourier-transform infra-red spectroscopy, Biochar: a guide to analytical methods 199 (2017).
[60] C.H. Chia, B. Gong, S.D. Joseph, C.E. Marjo, P. Munroe, A.M. Rich, Imaging of mineral-enriched biochar by FTIR, raman and SEM–EDX, Vib. Spectrosc. 62 (2012) 248–257.
[61] K.B. Cantrell, P.G. Hunt, M. Uchimiya, J.M. Novak, K.S. Ro, Impact of pyrolysis temperature and manure source on physicochemical characteristics of biochar, Bioresour. Technol. 107 (2012) 419–428.
[62] X.-Y. Liu, M. Huang, H.-L. Ma, Z. Zhang, J.-M. Gao, Y.-L. Zhu, X.-j. Han, X. Guo, Preparation of a carbon-based solid acid catalyst by sulfonating activated carbon in a chemical reduction process, Molecules 15 (2010) 7188–7196.
[63] J. Cui, Y. Li, Q. Jin, F. Li, Silica nanoparticles inhibit arsenic uptake into rice suspension cells via improving pectin synthesis and the mechanical force of the cell wall, Environ. Sci. Nano 7 (1) (2020) 162–171.
[64] S.S. Sahoo, V.K. Vijay, R. Chandra, H. Kumar, Production and characterization of biochar produced from slow pyrolysis of pigeon pea stalk and bamboo, Clean. Eng. Technol. 3 (2021) 100101.
[65] G.K. Gupta, M.K. Mondal, Mechanism of Cr(VI) uptake onto sagwan sawdust derived biochar and statistical optimization via response surface methodology, Biomass Convers. Biorefinery 13 (2) (2023) 709–725.
[66] M.E. González-López, C.M. Laureano-Anzaldo, A.A. Pérez-Fonseca, M. Arellano, J. R. Robledo-Ortíz, A critical overview of adsorption models linearization: methodological and statistical inconsistencies, Separ. Purif. Rev. 51 (3) (2022) 358–372.
[67] D. Mohan, C.U. Pittman, M. Bricka, F. Smith, B. Yancey, J. Mohammad, P.H. Steele, M.F. Alexandre-Franco, V. Gómez-Serrano, H. Gong, Sorption of arsenic, cadmium, and lead by chars produced from fast pyrolysis of wood and bark during bio-oil production, J. Colloid Interface Sci. 310 (1) (2007) 57–73.
[68] L. Han, L. Qian, R. Liu, M. Chen, J. Yan, Q. Hu, Lead adsorption by biochar under the elevated competition of cadmium and aluminum, Sci. Rep. 7 (1) (2017) 2264.

[69] I. Madsen, N. Scarlett, R. Kleeberg, K. Knorr, 3.9. quantitative phase analysis, Int. Tables Crystallogr (2019) 344–373.
[70] X. Cao, L. Ma, B. Gao, W. Harris, Dairy-manure derived biochar effectively sorbs lead and atrazine, Environmental Science & Technology 43 (9) (2009) 3285–3291.
[71] H. Lu, W. Zhang, Y. Yang, X. Huang, S. Wang, R. Qiu, Relative distribution of Pb2+ sorption mechanisms by sludge-derived biochar, Water Res. 46 (3) (2012) 854–862.